ACS OMEGA

Open Access

http://pubs.acs.org/journal/acsodf

Article

2D−2D Nanoheterostructure of an Exposed {001}-Facet CuO and MoS_2 Based Bifunctional Catalyst Showing Excellent Surface Chemistry and Conductivity for Cathodic CO_2 Reduction

Md Rajbanul Akhond, Md Jahidul Islam, Ahmad Irfan, and Ahmed Sharif*

Cite This: *ACS Omega* 2023, 8, 37353−37368

Read Online

ACCESS | Metrics & More | Article Recommendations | Supporting Information

ABSTRACT: A novel CuO-MoS_2 based heterostructure catalyst model system is proposed where a CuO nanosheet with exposed {001} facet with proper termination is the active surface for the catalysis and a MoS_2 nanosheet is the supporting layer. Density functional theory (DFT) calculations were performed to validate the model. The MoS_2 bilayer forms a stable heterostructure with {001} faceted CuO with different terminations exposing oxygen and copper atoms (active sites) on the surface. The heterostructure active sites with a low oxidation state of the copper atoms and subsurface oxygen atoms provide a suitable chemical environment for the selective production of multicarbon products from CO_2 electrocatalytic reduction. Furthermore, our heterostructure model exhibits good electrical conductivity, efficient electron transport to active surface sites, and less interfacial resistance compared to similar heterostructure systems. Additionally, we propose a photoenhanced electrocatalysis mechanism due to the photoactive nature of MoS_2. We suggest that the photogenerated carrier separation occurs because of the interface-induced dipole. Moreover, we utilized a machine learning model trained on a 2D DFT materials database to predict selected properties and compared them with the DFT results. Overall, our study provides insights into the structure−property relationship of a MoS_2 supported 2D CuO nanosheet based bifunctional catalyst and highlights the advantages of heterostructure formation with selective morphology and properly terminated surface in tuning the catalytic performance of nanocomposite materials.

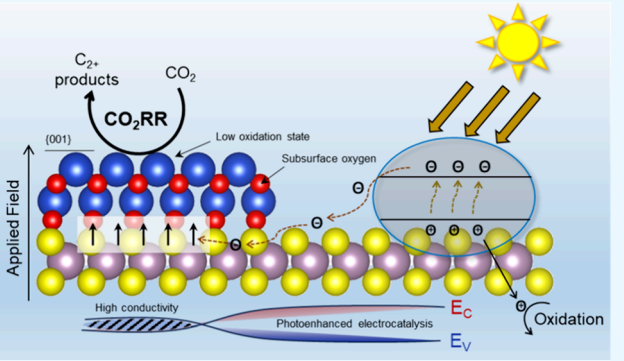

INTRODUCTION

According to the International Energy Agency, global energy consumption experienced a notable increase to 9938 million tons of oil equivalent in 2018. Notably, approximately 70% of this energy consumption was derived from fossil fuel sources, consequently leading to an unprecedented surge in carbon dioxide (CO_2) emissions surpassing 33 gigatons.[1] Moreover, two-thirds of the total electricity usage is expected to be generated from renewable resources by 2040,[2] and there is a potential requirement for long-term storage of this electricity for a reliable electric grid. The possibility of producing multicarbon (C_{2+}) products by reducing the amount of CO_2 presents opportunities to store renewable energy on a large scale and reduce carbon emissions.

Economically and energetically, C_{2+} hydrocarbons and oxygenates excel above C_1 compounds (e.g., methane or methanol). Plastics, textiles, and pharmaceuticals, to name a few, rely on C_{2+} hydrocarbons such as ethylene and propylene as fundamental building blocks. C_{2+} compounds also have higher energy density compared to C_1 products such as methane, meaning that they can supply more energy per unit volume. They are thus better suited for use in transportation and power generation among other energy-related applications. However, the inertness of CO_2, the high C−C coupling barrier, and the abundance of competing reactions leading to the creation of C_1 products make the synthesis of C_{2+} compounds more difficult.[3−5]

Copper-based materials, specifically Cu oxides (CuO_x), have garnered significant interest as catalysts for the electrochemical reduction of CO_2 (CO_2RR), and oxidized copper based catalysts have been observed to improve the selectivity and activity for C_{2+} products.[6,7] These materials exhibit broad chemical selectivity enabling the production of diverse multicarbon products including C_{2+} hydrocarbons and oxygenates. According to a report, researchers have identified a diverse range of 16 distinct types of products utilizing gas chromatography and nuclear magnetic resonance that can be

Received: July 19, 2023
Accepted: September 12, 2023
Published: September 25, 2023

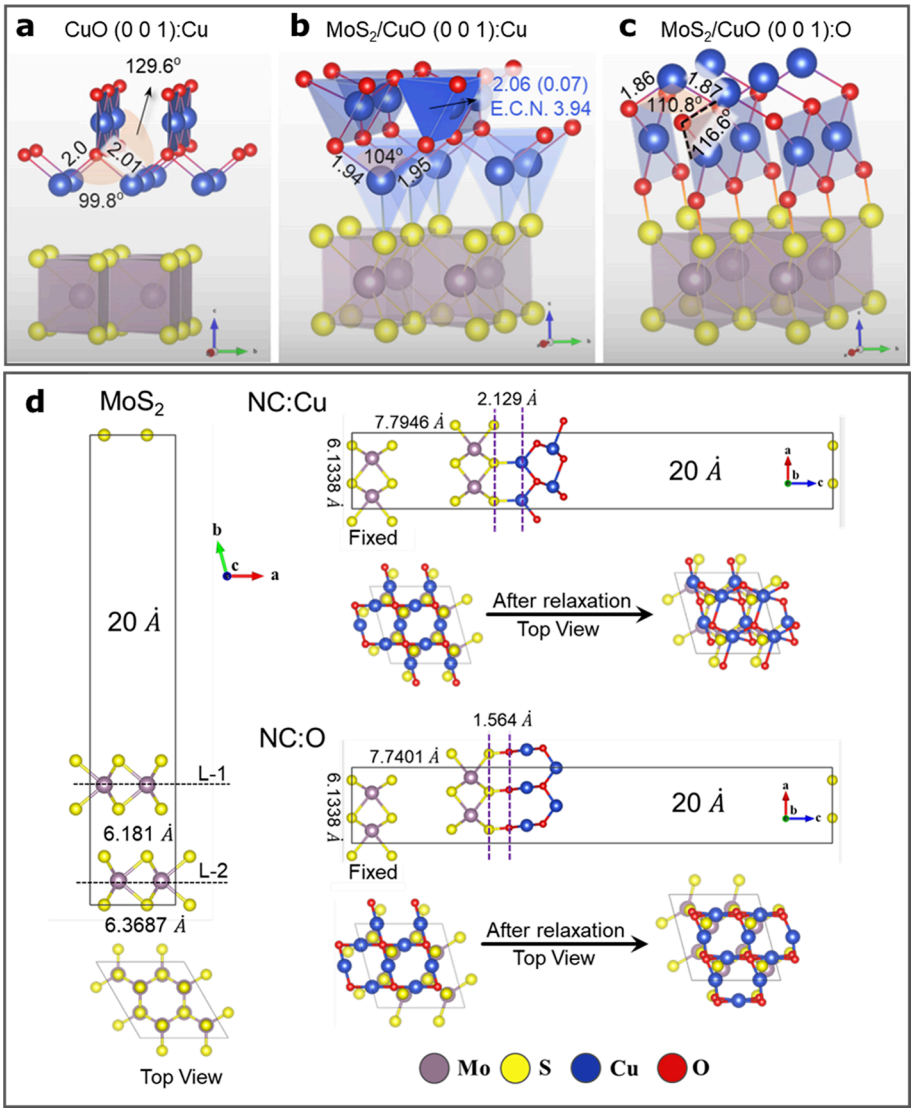

Figure 1. Supercell structure of the (a) CuO nanosheet with Cu termination before coming into contact with MoS_2; perspective view for the relaxed structures of (b) MoS_2-CuO (001: Cu) or NC: Cu and (c) MoS_2-CuO (001: O) or NC: O showing the CuO active layer. Top and side view of the slab and interface models of (d) pure MoS_2 and MoS_2-CuO heterostructure with Cu (NC: Cu) and O (NC: O) termination showing different interfacial distances after relaxation.

generated on copper catalysts via multiple proton-coupled electron transfer mechanisms.[8]

Different geometric shapes of CuO nanoparticles have been observed depending on precursor materials and synthesis routes, with each shape exhibiting a specific surface orientation. Their surface properties have been thoroughly investigated,[9] and activation of CO_2 on those surfaces has also been calculated theoretically using the DFT + U method.[10] Among them, the {111} oriented surface planes are the most stable, and CuO nanobelts (nanosheets) with (001) termination are less reducible than CuO nanoplatelets with (011) termination under a CO atmosphere.[11] Additionally, the {001} faceted CuO nanosheets have been synthesized by a simple hydrothermal approach with outstanding electrochemical performance.[12] More recently, researchers have synthesized (001) oriented CuO nanosheets with high C_{2+} production rate, good selectivity at industrially relevant current levels, and neutral pH;[13] however, with continuous reduction, these nanosheets agglomerate as metallic Cu dendrites. Thus, a good support material must be designed to increase its stability without sacrificing the catalytic properties of (001)-oriented CuO nanosheets.

MOS_2 can be a suitable choice for support material due to its good stability.[14] Moreover, MoS_2 with molybdenum-terminated edges has shown good CO_2 reduction performance with low overpotential and high current density.[15] MoS_2-CuO based nanocomposite (NC) heterostructures have been successfully synthesized by many authors, and these NCs have shown an exceptionally wide range of applications such as asymmetric supercapacitors, enhanced photocatalysis, pollutant degradation, photothermal therapy, and nonenzymatic glucose sensors.[16−20] However, synthesis methods used in those studies do not select for any specific morphology and proper surface termination of CuO nanostructures, and most of them are nanoparticles or nanoflowers with {111} surface termination, which is not suitable for CO_2RR, and the staggered type-II band alignment formed at the heterostructures shows low conductivity, decreasing electrocatalytic efficiency. Additionally, in MoS_2 and CuO based NCs, intercalation of CuO (001)-oriented slices into MoS_2 layers has been observed,

https://doi.org/10.1021/acsomega.3c05213
ACS Omega 2023, 8, 37353−37368

indicating that our proposed heterostructure model can be experimentally synthesized.[18,17]

To understand and design catalysts for electrocatalysis, the two most popular methods are in situ experimental methods and DFT calculations.[21] In this study, we used the DFT methodology with appropriate corrections for our proposed chemical system. Most of the DFT papers primarily focus on the thermodynamics of absorbate molecules onto catalysts' surface; however, it has been shown through on-chip microreactor measurements that the significance of electron injection at the interface between the catalyst and current collector as well as the intralayer and interlayer charge transport within the catalyst has more influence than thermodynamic energy considerations.[22] Thus, we focused our DFT calculations on understanding the atomistic electron transport mechanisms in our NC heterostructure catalyst models. Furthermore, machine learning techniques have become popular for direct structure to property prediction, accelerating conventional methods such as DFT. Thus, we performed machine learning inference for selected properties of our model catalyst systems using a model trained on the JARVIS-DFT 2D data set that is arranged by the Materials Genome Initiative (MGI) under the National Institute of Standards and Technology (NIST).[23]

In this study, we have shown that the CuO monolayer with exposed {001} facets can form a stable heterostructure with MoS_2, and this interaction does not alter the CuO surface chemistry negatively for selective CO_2 reduction to C_{2+} products and shows high electron transfer efficiency due to the synergy of different mechanisms with possible photo-enhanced electrocatalysis.

COMPUTATIONAL METHODOLOGY

Heterointerface Geometry. The crystal structure of CuO exhibits a monoclinic structure with $C2/c$ symmetry, as depicted in Figure S1b. The (001) crystal orientation allows for the occurrence of both Cu and O surface terminations.[24] Therefore, a CuO supercell was constructed in a manner that accurately represented the termination behavior (Figure S1d). The constructed CuO monolayer along the [001] direction has a structure where a Cu centered rectangle sits on top of a Cu−O zigzag layer with an angle of 129.6°. The Cu−O bond length is ∼2.0 Å, and they formed a 99.8° angle (Figure 1a).

The chosen base structure for modeling the bilayer molybdenum disulfide (MoS_2) is the 2-H MOS_2 polytype. This polytype exhibits a hexagonal structure with space group symmetry $P63/mmc$, as depicted in Figure S1a. In experiments where 2H-MoS_2 with flower-like nanospheres is synthesized, it mainly exhibits a preferential orientation of {002} planes.[25] In this study, MoS_2 nanoflowers (MS) were simulated using a 2 × 2 supercell consisting of two MoS_2 layers aligned along the direction [002] (Figure S1c). Chemical bonding occurs between molybdenum (Mo) and sulfur (S) atoms, resulting in the formation of a single layer. However, there is an absence of chemical bonding between these layers. Instead, adjacent layers are stacked in the [002] direction through the influence of van der Waals (vdW) forces.

In our study on nanocomposite heterostructures, we employed a monolayer of relaxed CuO structure. This structure exhibited both copper (CuO: Cu) and oxygen (CuO: O) terminations. Both heterostructures were modeled with identical lattice parameter values for a and b, along with a 20 Å vacuum in the c direction to prevent self-interaction errors. The values of a and b were determined to be 6.1338 Å, whereas variable c was measured to be 37.3742 Å. Additionally, the angle between a and b was found to be 105.038°, as depicted in Figure 1d. A (2 × 2) supercell of the CuO monolayer and MoS_2 bilayer with a lattice mismatch parameter of approximately 0.35% was utilized to construct the heterostructures. The lattice mismatch (α) was calculated using eq 1:

$$\alpha = \left(1 - \frac{2A_{MoS_2-CuO(Cu,O)}}{A_{MoS_2} + A_{CuO(Cu,O)}}\right) \times 100\% \quad (1)$$

where A_{MoS_2} and A_{CuO} are the surface areas of pure slabs and A_{MoS_2-CuO} is the overlapping area of the composites. Figure 1d illustrates the relaxed structures of the heterostructures pertaining to both Cu and O terminations of CuO. These structures are denoted as NC: Cu and NC: O with exposed O and Cu atoms on surface, respectively, in subsequent discussions. Multiple candidates for global lowest energy configuration can be extracted through lattice vector matching[26] or from other latest methods such as the nonperiodic screening approach.[27] With the assumption that our local minimum configuration is close to that of the global minimum, the conclusion derived in the later sections of the paper will hold without loss of any generality.

After ionic relaxation, the CuO monolayer was reconstructed significantly. For NC: Cu, the previous rectangular structure has morphed into a tetrahedron with Cu atoms at the center and O atoms at the vertices. The average bond distance in the tetrahedron is 2.06 Å with a bond distortion index of 0.07, and it has a near perfect effective coordination number of 3.94. The zigzag structure has formed a triangular plane with a Cu atom at the center and two O atoms and a S atom, forming the three vertices of the triangle. The Cu−O bond length decreased, and the angle between them increased (Figure 1b). For NC: Cu, the changes are not that drastic as the overall morphology of the CuO monolayer has not changed much with slight changes in angles and bond lengths, which is also evident from the top view after relaxation (Figure 1d). Moreover, the subsurface O atoms have come closer to the surface Cu atoms due to the decreased Cu−O bond length and increased angle in the zigzag structure (Figure 1c). This structural change is very important, as these exposed Cu atoms with subsurface O atoms form the basis of enhanced CO_2RR that will be discussed later.

Calculation Details. The present study employed the Vienna Ab Initio Simulation package (VASP) code[28] to conduct first-principle DFT calculations. The projector augmented wave (PAW) method[29,30] as implemented in the code captures the valence electrons and core ion interactions, which was originally proposed and utilized by Blöchl[30] and developed by Kresse.[31] The valence electron configurations that were investigated include Mo (4s2 4p6 5s1 4d5), S (3s2 3p6), Cu (3d10 4s1), and O (2s2 2p4). To address the issue of band gap underestimation in highly correlated materials, the analysis of CuO in this study employed the Hubbard DFT + U correction scheme. This correction scheme was initially introduced by Anisimov et al.[32] The aforementioned methodology has been extensively employed in the investigation of various transition metal compounds.[33,34] There exist alternative computation methods that offer higher accuracy, such as the hybrid functional (HSE06)[35] and GW functional,[36] albeit at a higher computational cost.

https://doi.org/10.1021/acsomega.3c05213
ACS Omega 2023, 8, 37353−37368

The approximated functional employed was the Perdew–Burke–Ernzerhof (PBE) functional using the generalized gradient approximation (GGA).[37] In all calculations, a uniform cutoff energy of 520 eV was employed for the plane-wave basis set. The Monkhorst–Pack scheme was used to generate a gamma-centered K-point grid automatically. The k-point reciprocal space sampling was conducted by using a spacing of 0.03 between adjacent points. To optimize the geometry, ionic relaxation was conducted until the energy variations and atomic forces reached values below 10^{-7} eV and 0.03 eV/Å, respectively, and the cell volume was kept fixed. A Hubbard potential with an effective energy of U_{eff} = 7.14 eV was introduced to the highly localized 3d orbitals of copper based on the value reported in the relevant literature.[38] DFT-D3 (semiempirical-based)-type van der Waals (vdW) corrections were used in this study to account for dispersion errors.

The inference of electronic and optical properties was performed using the JARVIS-ML model that was trained on the JARVIS-DFT data set with classical force-field inspired descriptors (CFID).[23] This data set contains 674 nonmetallic exfoliable 2D materials with 226,779 possible vdW heterostructures. Predictions from the model were then compared to our DFT values.

Van der Walls Correction. Van der Waals corrections are required to account for the interactions between layers in 2D heterostructures. These corrections are typically accurate and can be applied using interatomic potentials or exchange correlation functionals such as DFT-D and vdW-DF. In the present study, the DFT-D3 method, an updated version of DFT-D, was utilized to conduct density functional theory calculations with van der Waals correction.[39] This implementation is based on interatomic potentials of the form $C^6 \cdot R^{-6}$, which is added to the total Kohn–Sham energy. The R^{-6} term accounts for the long-range dispersive interactions between atoms, and the C^6 coefficient represents the strength of the interaction.

From Figure 2a, it can be observed that distance between MoS_2 layers decreased (7.23 to 6.18 Å) after using the dispersion corrected methods. This decrease can be attributed to the fact that the D3 scheme successfully captured the van der Waals interactions between the layers, which counteracted the repulsion between the layers. The decreased interlayer distance also increases the interlayer coupling between them, which mainly affects the states near the Γ point. This strong coupling effect near the Γ point is due to the combination of Mo d-orbitals and S antibonding p^z-orbitals on the S atoms.[40] Because of this effect, the indirect band gap (Γ → K) with dispersion correction is 1.17 eV (Figure 2c), which is lower than the band gap of 1.52 eV (Figure 2b) without any correction. The conduction band states at the K-point primarily originate from the localized d-orbitals on the Mo atoms and are situated in the center of the S–Mo–S sandwich structure.[41] These states are comparatively unaffected by interlayer coupling and thus do not play any role in the decreased band gap. This correction scheme also has an important effect on the heterostructure energetics, as can be seen from the higher contribution from dispersion energy (E_d) compared to unmodified MoS_2 (Table 1).

RESULTS

Structures and Interaction Energies. Following the relaxation process in the case of NC: Cu, the distance between the MoS_2 layer and CuO was calculated to be 2.129 Å.

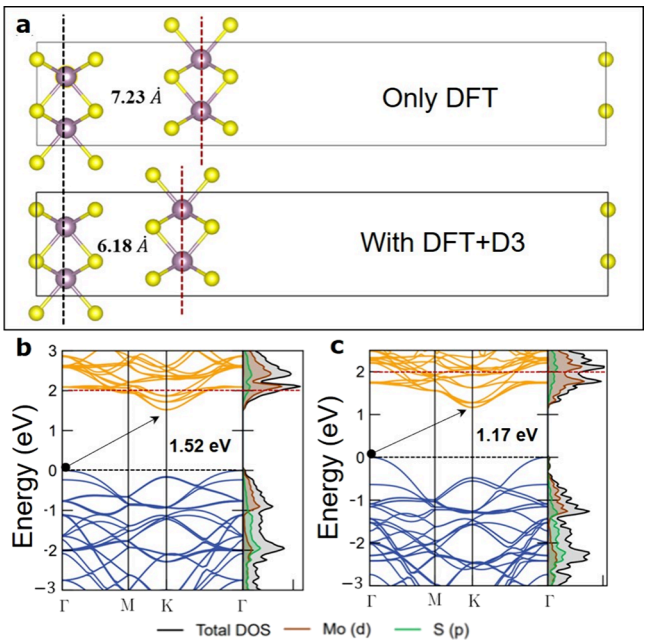

Figure 2. Effect of D3 based dispersion correction on (a) layer distance in the optimized bilayer MoS_2 structure and band structure (DOS) calculation (b) without and (c) with dispersion correction.

Table 1. Interfacial (Surface) Interaction Energies, Bonding Energy, Work Function, Schottky Barrier Height and Intrinsic Electric Field for MoS_2 and NC: Cu, NC: O Heterostructures

configurations	interaction energies (eV) E_γ/E_b	E_d	γ/W_{ad} (J m^{-2})	φ (eV)	SBH (eV)	E_{in} (eV)
MoS_2	−1.06	5.48	0.015	5.138		
NC: Cu	−4.8	8.68	0.132	5.279	0.2	3.07
NC: O	−0.879	8.63	0.026	5.280	0.62	2.88

Additionally, the distance between the MoS_2 layers increased from 6.181 to 7.7946 Å. In the case of NC: O, the interfacial distance between the two heterostructures decreased to 1.564 Å, whereas the interlayer distance of MoS_2 decreased from 7.7946 to 7.7401 Å, as depicted in Figure 1d.

When two MoS_2 layers are separated, two extra surface areas are generated. Thus, the surface energy can be calculated using eq 2:

$$\gamma = \frac{-(E_{MoS_2-bulk} - E_{MoS_2-slab})}{2A} \quad (2)$$

where $E_{MoS_2\text{-bulk}}$ and $E_{MoS_2\text{-surface slab}}$ are the total energy of the bulk MoS_2 and bilayer slab of MoS_2, respectively, and A is the area of the newly created surfaces.

The energy required to separate two heterogeneous crystal slabs is defined as the interfacial binding energy (E_b), and it can be calculated using eq 3:

$$E_b = E_{MoS_2-CuO(Cu:O)} - (E_{MoS_2} + E_{CuO}) \quad (3)$$

where $E_{MoS_2\text{-CuO(Cu: O)}}$, E_{MoS_2}, and $E_{CuO}$are the total nanocomposite energy for both terminations, MoS_2 bilayer slab, and CuO slab after contact, respectively. The greater the negative value of E_b is, the higher is the interlayer adhesion. Furthermore, the evaluation of the stability involved the

https://doi.org/10.1021/acsomega.3c05213
ACS Omega 2023, 8, 37353−37368

Table 2. Distance between MoS_2 Layers and Average Bond Distance between Mo−S, Cu−S, O−S, and Cu−O Bonds Located near the Surface (interface) Sites for MoS_2 and NC: Cu, NC: O Heterostructures

configurations	MoS_2 interlayer distance (Å)			average bond distance near (surface) interface (Å)			
	this work	exp.[20]	theory[40]	Mo−S	Cu−S	O−S	Cu−O
MoS_2	6.18	6.2	7.884	2.411			
NC: Cu	7.79	7.2		2.474	2.131		1.951
NC: O	7.74			2.422		1.577	2.152

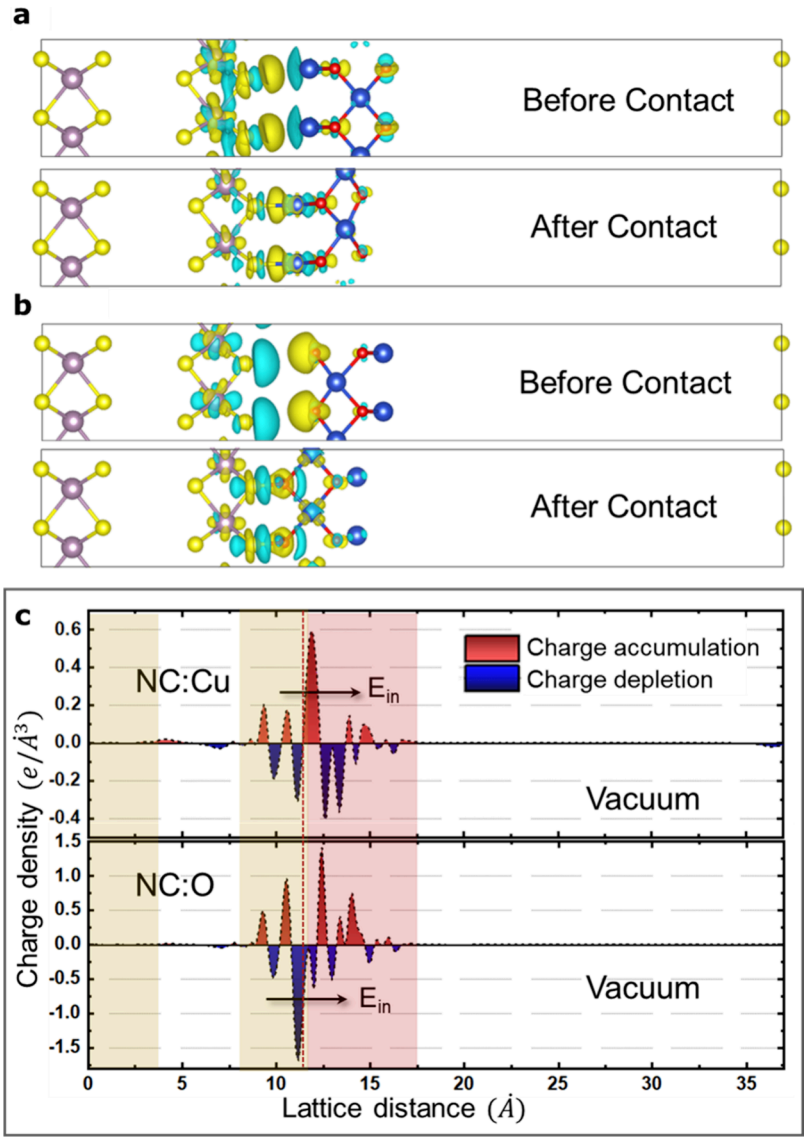

Figure 3. Spatial mapping of charge density differences before and after contact (3D plot, yellow = charge accumulation and blue = charge depletion) of (a) NC: Cu and (b) NC: O and average line density differences after contact for (c) both heterostructures.

utilization of the work of adhesion (W_{ad}), which takes into account the distinct cross-sectional areas of the slab models. W_{ad} is defined as the interfacial binding energy needed (per unit area) to reversibly separate the interface into two free surfaces (eq 4):

$$W_{ad} = -\frac{E_b}{A} \tag{4}$$

Here, interfacial binding energy is expressed in joules, and contact area A is in m^2. Apparently, the work of adhesion exhibited a similar trend as the binding energy.

Table 1 displays that the surface and binding energies have negative values, signifying their stability. Notably, NC: Cu stands out as the most stable structure with the lowest binding energy of −4.8 eV. The increase in the MoS_2 interlayer distance due to the incorporation of CuO has been observed experimentally (Table 2). Moreover, according to previous research, adsorption distances between 2.0 and 2.5 Å are indicative of chemical interactions.[42] On the basis of this criterion, all studied systems exhibit chemisorption behavior.

Charge Density Difference and Bader Charge Analysis. We conducted calculations of charge density differences to gain a deeper insight into the evolution of

https://doi.org/10.1021/acsomega.3c05213
ACS Omega 2023, 8, 37353−37368

electronic structure as a result of interfacial interaction (Figure 3). The charge density difference was computed using eq 5:

$$\Delta\rho_{\text{difference}} = \rho_{\text{total}} - \sum \rho_{\text{i}} \quad (5)$$

where ρ_{total} and $\sum\rho_{\text{i}}$are the total charge density and summation of crystal fragments' charge density, respectively.

As can be seen from Figure 3a for NC: Cu, before coming into full contact, the charge density has accumulated near the MoS_2 side of the interfacial vacuum region, and charge depletion has occurred at the CuO side. In the case of NC: O, the situation has fully reversed as charge accumulated near the CuO side and depleted near the MoS_2 side (Figure 3b). This inversion can be easily explained as sulfur is more electronegative than copper and less electronegative than oxygen (2.4 vs 3.5). This inverse charge redistribution behavior between MoS_2 and CuO creates oppositely charged poles, which in turn can cause these slabs to come into contact more easily.

Upon contact, NC: O shows greater charge separation than NC: Cu due to strong S−O bonds formed at the interface, driving charge transfer. Charge accumulation on the CuO side extends 0.87 Å for NC: Cu and 2.2 Å for NC: O, whereas charge depletion on the MoS_2 side extends 3 Å for NC: Cu and 3.22 Å for NC: O. These polarized interfaces can serve as active sites for redox reactions in electrocatalytic[43] and photocatalytic[44] reactions. Moreover, from the average charge density difference plots, the charge redistribution magnitude in the case of NC: O is around three times greater than that of NC: Cu. This difference will be more obvious from the amount of total electron transferred calculated through Bader charge analysis method in the following paragraph.

Bader charge analysis, also known as the atoms-in-molecules theory, involves the partitioning of molecules into individual atoms by using zero flux surfaces. A surface that exhibits zero flux is characterized as a two-dimensional surface where the density of electric charge experiences a minimum value upon traversing the surface. The Bader charge of an atom refers to the aggregate charge that exists within the atomic volume, also known as the Bader volume.[45] As charge density calculated from VASP code only contains valence electrons, the reference charge states have been taken as 14, 6, 11, and 6 for Mo, S, Cu, and O, respectively.

For NC: Cu, the Cu atoms on the first layer have lost on average ∼1 electron, and for the second layer, it is higher at around 1.11 electrons. In comparison, for NC: O, the loss of electrons is less around 0.58 and 0.8 for the first and second layers of Cu atoms (Figure 4a,c). Thus, the oxidation state of Cu atoms is a gradient, lower at the surface layer and higher toward the bulk. For Mo atoms near CuO, they lost around 1 and 1.1 electrons for NC: Cu and O, respectively. In the case of the anions, O atoms in the first layer have gained around 0.77 and 1.03 electrons for the NC: Cu and O, respectively, and for the second layer, they have gained around 0.95 and 1.8 electron) (Figure 4b,d). In this case, the oxidation state trend is similar to the cations, low at the surface and high at the bulk. For the interfacial S atoms, they gained on average 0.82 and 0.94 electrons for NC: Cu and O, respectively.

In the previous section, electron transfer between the atomic species was discussed. In terms of electron transfer between different layers, if the electrons from Bader analysis for all the atoms in a slab are summed up after the contact and compared with the reference number of total electrons in the slab before the contact, the electron transfer between the slabs can be

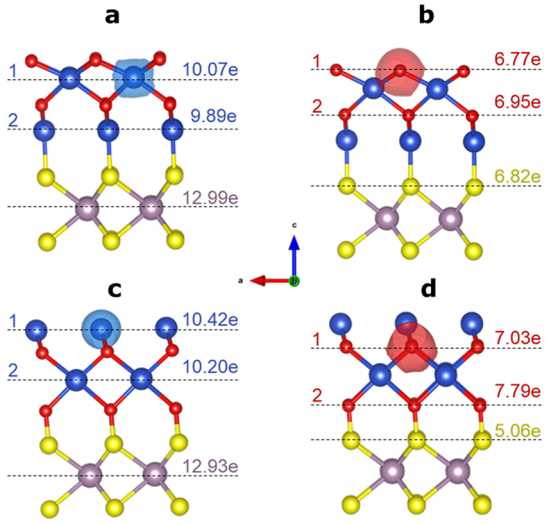

Figure 4. Bader charge analysis for (a) cations (Cu, Mo), (b) anions (O, S) for NC: Cu and (c) cations, (d) anions for NC: O with isosurfaces indicating the corresponding Bader volume.

determined. According to the calculations, 1.28 electrons are transferred from CuO to MoS_2 for NC: Cu on average. For the case of NC: O, the transfer direction was reversed, and 5.74 electrons were transferred from MoS_2 to CuO. This transfer amount can be normalized with respect to the area, and the electrons transferred per unit area were 0.035 and 0.158 $e.\ Å^{-2}$ for NC: Cu and O, respectively.

From the previous section and charge difference analysis, it is obvious that for the NC: O system, the MoS_2 slab was acting as electron donor and the CuO slab as acceptor. However, for the NC: Cu system, the case is not as simple. From the charge difference calculation, the electron charge density had accumulated at the center of the Cu−S bond, and the charge transfer is very localized at the interface. Thus, there is a possibility that Bader charge analysis has counted this accumulated charge for the S atoms at the interface, and as a result, the MoS_2 slab seems like an electron acceptor in this case. Moreover, as the work function of both CuO:(Cu/O) models are larger than the MoS_2 bilayer, electrons are directed spontaneously from the MoS_2 bilayer to the CuO layer (Figure S5); thus, we can assume for both cases an n-type Schottky contact considering the anomaly. According to the Schottky−Mott rule, the n-type Schottky barrier height (SBH) can be calculated using eq 6:

$$\text{SBH} = E_{\text{CBM}} - E_{\text{F}} \quad (6)$$

where E_{CBM} is the conduction band minimum of the MoS_2 bilayer and E_{F} is the Fermi level of the heterostructure. According to the calculation presented in Table 1, the NC: Cu and O have SBHs of 0.2 and 0.62 eV, respectively. For comparison, MoS_2 and graphene (MS-G) and SWSe and graphene (SWSe -G) have n-type SBHs of 0.49 and 0.35 eV, respectively.[46]

From the charge difference calculation, it has been observed that because of electron transfer between MoS_2 and CuO slab, an intrinsic electric field (E_{in}) had been formed. This intrinsic field can be quantified by the following formula (eq 7):

$$E_{\text{in}} = \varphi_{\text{CuO}} - \varphi_{\text{NC:(Cu,O)}} \quad (7)$$

https://doi.org/10.1021/acsomega.3c05213
ACS Omega 2023, 8, 37353−37368

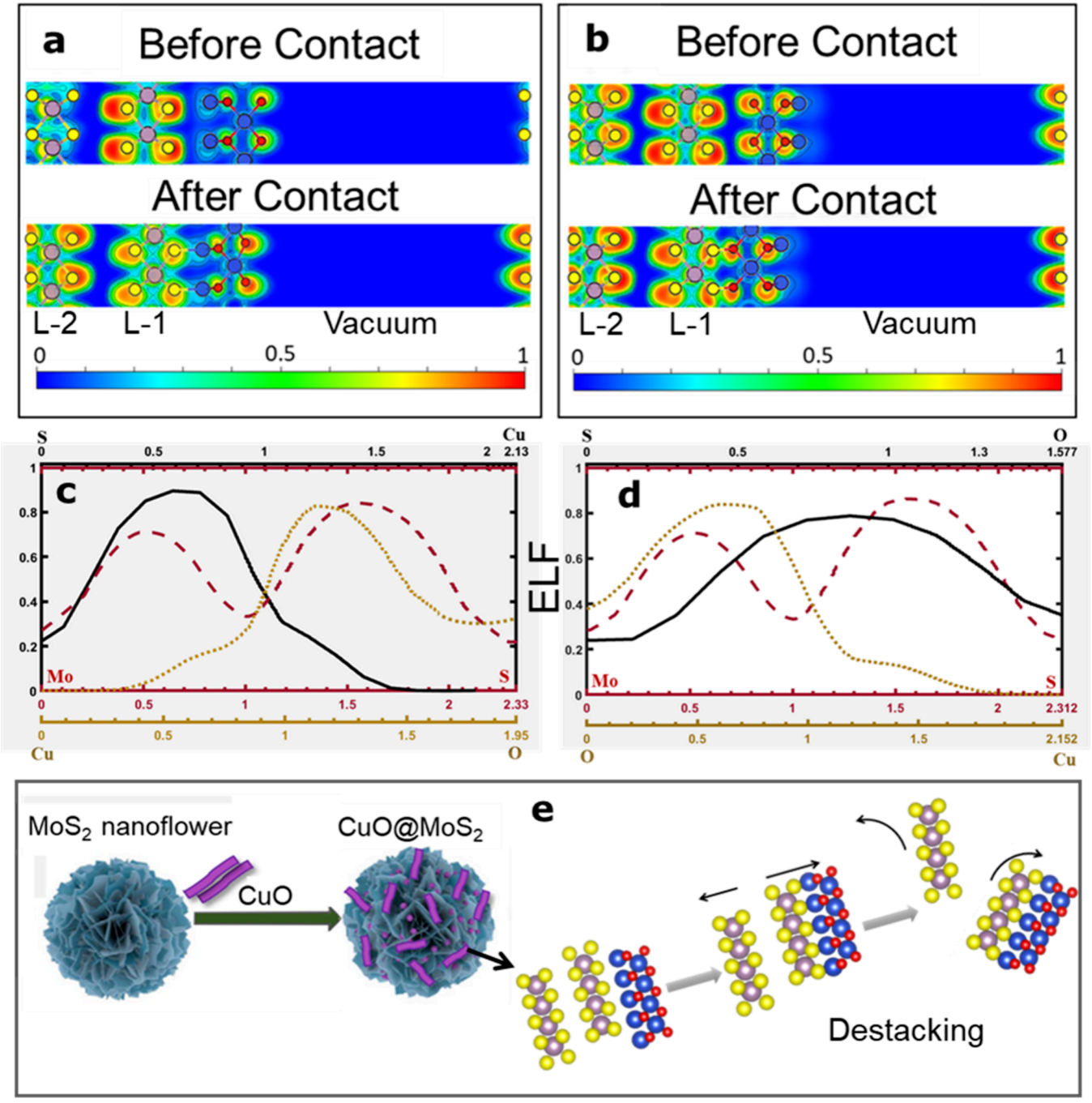

Figure 5. 2D color map of ELF before and after the contact between MoS_2 (002) and (a) Cu (001): Cu and (b) Cu (001): O. ELF profile of the interfacial regions between neighboring atoms of S−Cu, Mo−S, and Cu−O for (c) NC: Cu and S−O, Mo−S and O−Cu for (d) NC: O. (e) Schematic illustrating the destacking of 2H-MOS_2 layers due to interaction with CuO. See Figure S2 for the 3D ELF isosurfaces.

Here, $\varphi_{NC:\,(Cu,\,O)}$ and φ_{CuO} are the work functions of NC: (Cu, O) heterostructures and CuO slab, respectively. The E_{in} is slightly higher for NC: Cu compared to NC: O (Table 1). The SWSe-G heterostructure shows a much lower intrinsic field (0.81 eV) due to similar electron transfer.

Interfacial Bonding Characteristics. The measurement of electron localization in atomic and molecular systems, known as ELF, is determined by the probability density of locating another electron with the same spin near the reference electron and is connected to the electron density. It is also a differential scalar field in three-dimensional space, which means that it is a function that assigns a scalar value to each point in space, and its definition is presented in eq 8:

$$n(r) = \frac{1}{1 + \chi(r)} \tag{8}$$

$$\chi(r) = \frac{\frac{1}{2}\sum_{i=1}^{N}|\nabla\psi_i(r)|^2 - \frac{1}{8}\frac{|\nabla\rho(r)|}{\rho(r)}}{D_h(r)} \tag{9}$$

$$D_h(r) = \frac{3}{10}(3\pi^2)^{2/3}\rho(r)^{5/3} \tag{10}$$

https://doi.org/10.1021/acsomega.3c05213
ACS Omega 2023, 8, 37353−37368

The electron localization $D(r)$, the numerator in eq 9, is the difference between the kinetic energy density and the bosonic kinetic energy density. The ψ_i represents Kohn–Sham orbitals, and $\rho = \sum_i |\psi_i|^2$ stands for electron charge density. The uniform electron gas $D_h(r)$ is defined as eq 10. This ELF technique can be used to separate chemical type bonding from physical binding.[47]

When $n(r)$ is greater than 0.7, electrons are considered localized with core or bonding regions or lone pairs, whereas electron localization is similar to electron-gas and characteristic of metallic bonds when $n(r)$ ranges from 0.2 to 0.7. Between the two MoS_2 layers, the electron localization near the sulfur atoms of the L-1 before contact is high compared to the L-2. The situation has reversed after contact, and thus, the net localization has decreased. This phenomenon is more prevalent for the NC: Cu system (Figure 5a,b). According to Bader analysis, the sulfur atoms of L-1 gained on average less electron compared to L-2 (0.51 vs 0.58 for NC: Cu and 0.56 vs 0.58 for NC: O) with respect to reference. Thus, the L-1 sulfur atoms along the MoS_2 bilayer vdW interface have less polarizable electron cloud as the lower count of available electrons is more tightly bound to the sulfur nucleus. As the interaction between MoS_2 layers is of a vdW origin and the magnitude of the attractive vdW force depends on the polarizability of electron cloud, the vdW attraction between MoS_2 layers had decreased, and as a result, the interlayer distances had increased after the introduction of CuO. The NC: Cu system has comparatively less polarizable sulfur atoms, and as a consequence, it showcases a larger interlayer distance compared to NC: O (Table 2). This property can be used to destack the MoS_2 monolayer from bulk nanoflowers by sonicating MoS_2/CuO solution as illustrated in Figure 5e. The formed nano-heterostructure will be more active for catalytic reactions due to the increased surface area.

For both NC: Cu and O systems, a centered delocalized zone can be observed with an ELF value of around 0.5 due to Mo carrying σ-aromaticity inside every hexagonal ring of the MoS_2 structure.[48] The bond type between Mo and S is mixed ionic–covalent.[49] However, separation of localized electron density can be observed in both heterostructures, and a non-nuclear minimum of around 0.35 at 1 Å from Mo atom can be observed (Figure 5c,d). This bond tearing can be due to the increased bond length of Mo–S for both systems (Table 2) resulting from the interfacial interaction with CuO. The interfacial bond between S and Cu in the NC: Cu system has a bond length of 2.131 Å, and the localized electron cloud is near the S atom with a maximum ELF value of around 0.9 at 0.6 Å from the S atom, making the Cu–S bond strongly ionic (Table 2 and Figure 5c). On the other hand, the interfacial bond between O and S in the NC: O system is smaller compared to NC: Cu with a value of 1.577 Å, and mostly a diffused covalent type bond can be deduced from the maximum ELF value of around 0.8 at 0.9 Å from the S atom (Table 2 and Figure 3d). In case of the Cu–O bond for both systems, they are both ionic with maximum electron localization near the O atom, and this localization is more dominant for surface O atoms in the case of the NC: Cu system as can be seen from the after-contact structure compared to the before-contact structure in Figure 5a.

Electronic Structure. To acquire a deeper understanding of the electronic characteristics of MoS_2/CuO heterostructures, with particular focus on the impact of interface and termination type on the electronic structure, band structure and density of states (DOS) calculations were conducted and are presented in Figure 6.

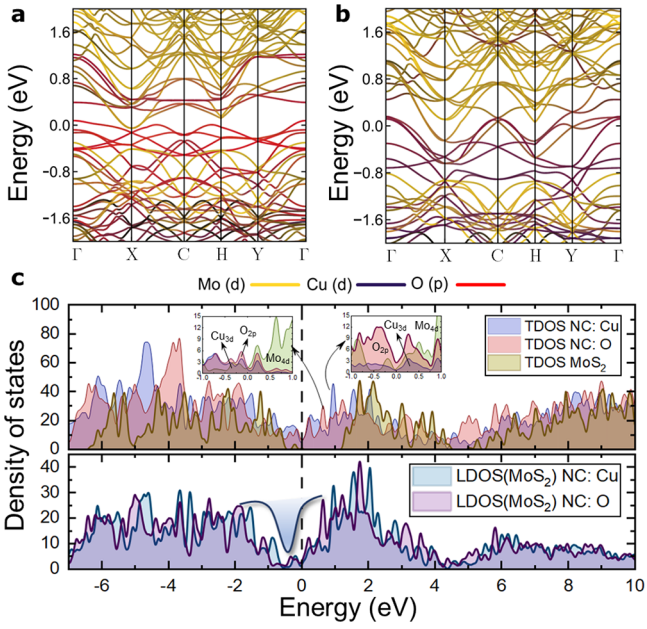

Figure 6. Band structures showing the atomic band projection for (a) NC: Cu and (b) NC: O heterostructures with orbital projected DOS (PDOS) in the inset and (c) total density of states (TDOS) for all models and local density of states (LDOS) of NC: Cu and NC: O. The Fermi energy level is set at zero.

The NC: Cu and NC: O heterostructures both show a metallic behavior due to the formation of states near the Fermi level as can be seen from the band structure and total density of states (TDOS) (Figure 6a–c), and these states are dominated by O-2p orbitals in the case of NC: Cu; however, these orbitals have little influence on NC: O as can be seen from the projected states on to Mo-4d, Cu-3d, and O-2p orbitals (Figure 6c inset). Moreover, these states near the Fermi level of NC: Cu mainly come from the O atoms on the surface of the heterostructure (Figure S3a). The interfacial atoms Cu–S for NC: Cu and O–S for NC: O have little contribution toward those states as they mainly constitute the states deep into VBM and CBM (Figure S3b,c). Moreover, the interactions with these active O-2p orbitals have modified the Mo-4d orbitals for both heterostructures, especially as they have merged from both band edges to form a continuous band. For experiments where MoS_2 is the main constituent and CuO is used as a modifier, the electronic properties are mainly dominated by MoS_2, with the MoS_2–CuO interactions playing an important role in modifying the base electronic structure and the influence of these interactions becoming more visible with increasing CuO content. To comprehend the impact of the interface formation on the electronic properties of MoS_2, we projected the bands onto the MoS_2 slab to derive the local density of states (LDOS), which had a profound effect (as demonstrated in Figure 6c LDOS). The most prominent characteristic of this projected DOS is that there is limited overlap between the CBM and the VBM bands. Although the GGA + U functional used in this study led to an underestimation of the calculated band gaps of MoS_2 and CuO (001: Cu, and O), the relative trends between these

https://doi.org/10.1021/acsomega.3c05213
ACS Omega 2023, 8, 37353–37368

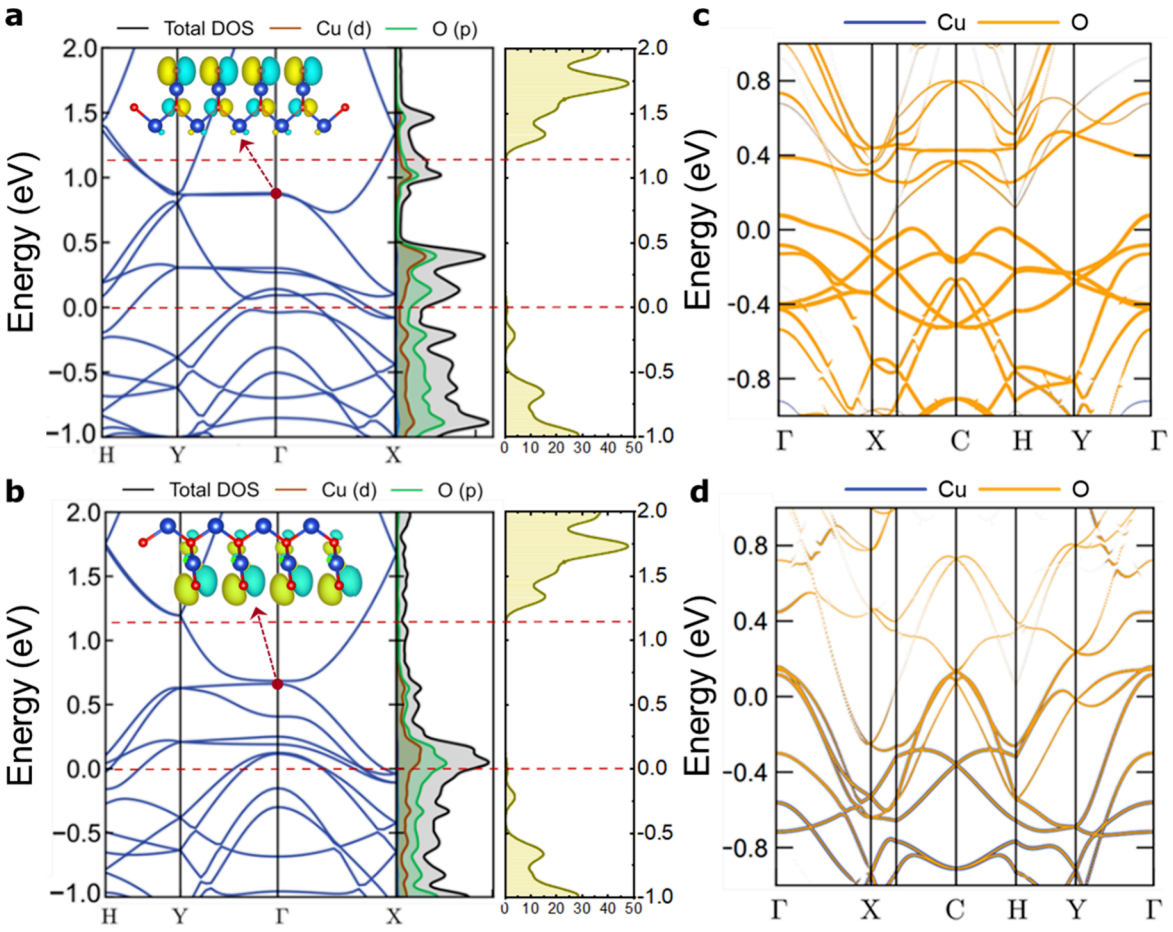

Figure 7. Band structures showcasing the metallicity of CuO (001) along with isosurfaces of the electron wave function corresponding to bands inside the conduction band, sampled at the Γ point, for the slab model of (a) CuO (001): Cu and (b) CuO (001): O along with VBM and CBM of pristine MoS_2 for reference. Band projected onto the CuO layer for (c) NC: Cu and (d) NC: O nanocomposite heterostructures. The Fermi energy level is set at zero.

values remain valuable. This metallicity is mainly due to the hybridization between the O-p orbital and the modified d orbital from Mo sites, and from the charge redistribution analysis, it was evident that these interactions do not penetrate deep into the MoS_2 layers. As a result, there is a gradual transition from metallic CuO toward semimetallic MoS_2 layer(s) near the MoS_2−CuO heterointerface and ultimately to the bulk semiconductor like behavior of MoS_2. Another important observation can be made that the LDOSs have shifted toward lower energy, and this is more prominent for NC: O due to the existence of a stronger interfacial dipole than NC: Cu as calculated previously.

Metallic CuO Modulated Electrocatalysis. From the previous section, the electronic activity near the Fermi level (which is important for understanding catalytic processes) is mainly due to CuO, more specifically the 2p orbital in CuO. To fully understand the metallicity, we calculated the projected band structures for only CuO slabs with {001} facets (Cu and O terminations in Figure 7a,b). As can be seen from the plot, they both show metallicity on their own. The states inside the conduction channel are mainly due to the surface oxygen atoms, as can be observed in the isosurface wave function plot corresponding to the energy bands. Surface atomic site induced metallicity has been previously observed in similar CuO structures and is demonstrated to be an authentic electronic effect at the surface, unaffected by surface unit-cell size and symmetry.[50] The CuO (001): O also shows metallicity; however, the DOS in the conduction band region is very low compared to CuO (001): Cu. Unlike the Cu termination, the chemical environment of these O atoms will be strongly modified when MoS_2 is brought into contact, forming a strong covalent bond that will influence the metallicity. Additionally, from the reference band edges of pristine MoS_2, these O induced conductive channels sit right between the VBM and CBM of MoS_2 and, along with hybridized Mo 4-d orbitals, create a continuous conduction channel for the metallic heterostructure. A similar level of metallicity of CuO persists even after the formation of the heterostructure as can be observed from the projected bands in Figure 7c,d with the CuO slab showing the presence of more conduction channels in the NC: Cu heterostructure compared to NC: O.

Optimizing the electron transport path and minimizing interfacial resistance between the catalyst/cathode and interlayer interface are crucial, as the transfer of charges within the catalyst system holds greater significance than thermodynamic energy considerations. The matter of the electron transport path is trivial for this case. Thus, the cause of interfacial resistance, which is mainly due to two physical phenomena, resistance due to (I) Schottky barrier height (SBH) and (II) electron tunneling through the interfacial electrostatic potential barrier, will be presented.

https://doi.org/10.1021/acsomega.3c05213
ACS Omega 2023, 8, 37353−37368

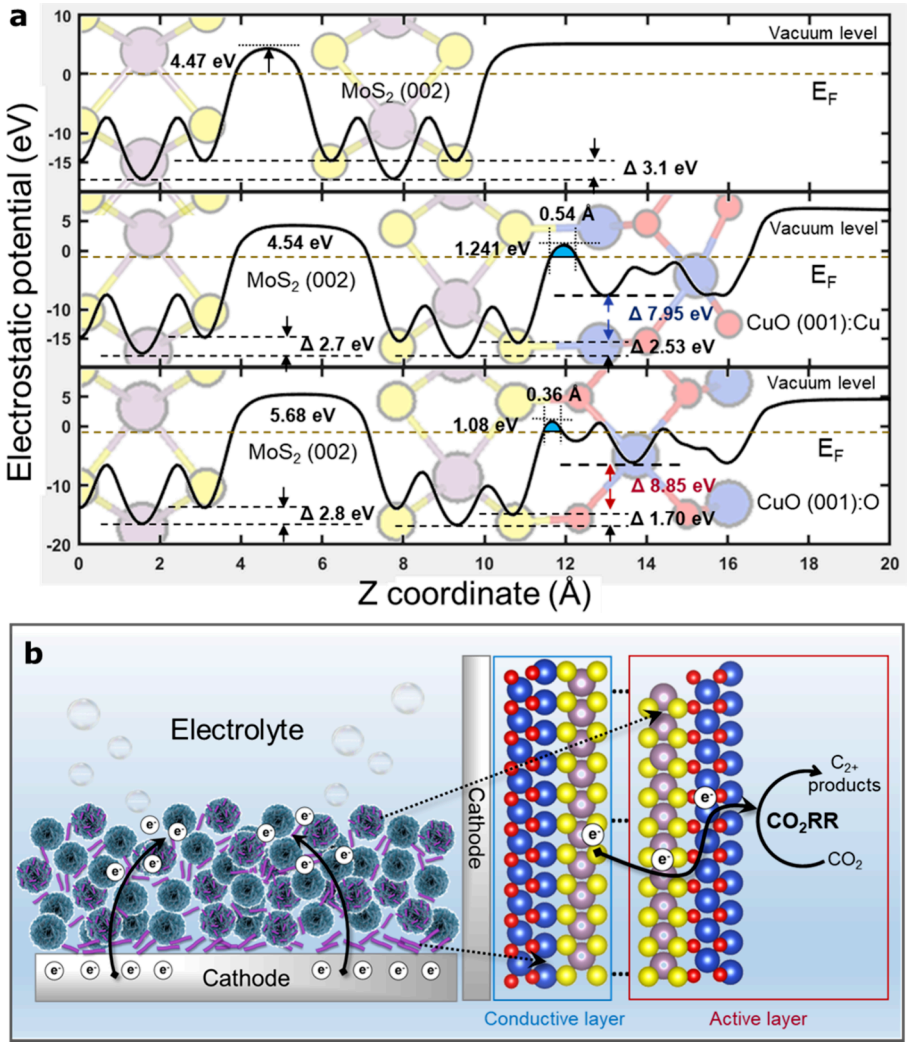

Figure 8. Electrostatic potential profile for (a) MoS_2 slab, NC: Cu, and NC: O models along the *c* direction. The Fermi level is with respect to the vacuum level, which is at 5 eV for the models. The electron tunneling barrier is shaded in blue (width, w_t, height, Φ_t). (b) Schematic showing the CuO modulated conductive layer-active layer-assisted electrocatalytic CO_2RR mechanism of MoS_2-CuO.

Because of chemisorption between MoS_2-CuO and the presence of electronic states near the Fermi level, there are no large vdW gap and SBH induced barrier. However, tunneling barriers exist because of electrostatic potential differences, which are shown in Figure 8a. The barrier has a width (w_t) of 0.54 and 0.36 Å and a height (Φ_t) of 1.241 and 1.08 eV for NC: Cu and NC: O, respectively, marked blue in the electrostatic potential profile. This induces a tunneling resistivity due to tunneling barrier probability (PTB),[46] and it can be defined by eq 11:

$$P_{TB} = e^{-2w_t/\hbar\sqrt{2m\Phi_t}} \tag{11}$$

where m is the mass of a free electron and $\hbar$ is the reduced Planck constant. To understand the tunneling barrier, eq 11 can be simplified to obtain a comprehensive factor: $C = w_t^2\Phi_t$. It is evident that a lower C value is beneficial owing to the increased likelihood of a larger tunneling barrier probability and a decline in tunneling resistivity. Regarding this metric, NC: O has lower value of C (0.14) compared to NC: Cu (0.36). For comparison, the semimetal−semiconductor heterostructure Bi and MoS_2 has a tunneling width of 1.66 Å, a height of 3.6 eV, and a corresponding C value of 9.9 that is very large compared to our models.[51] This is mainly due to the vdW interactions between MoS_2 and bismuth (Bi). A slight contrast exists between the mechanism in which the two structures avoid gap state induced Fermi-level pinning. In the case of MoS_2-Bi, the Fermi level of MoS_2 is shifted into the conduction band, yielding a degenerate MoS_2 in contact with Bi. However, in the case of MoS_2-CuO, the band edge states, which are mainly composed of Mo-4d orbitals, are hybridized with surface O-2p orbitals from CuO, resulting in a continuous band from the VBM to CBM. Without this hybridization, the d orbitals can form discrete gap states in case of direct contact with the metal electrode. Thus, MoS_2-CuO (001) based heterostructures can be used as both conductive and active layers for electrocatalysis depending on the termination of CuO. The activity of this layer can be further enhanced by using the photoactive characteristic of MoS_2, which will be discussed in the next section.

Directional Photoenhanced Electrocatalysis. We have calculated the optical properties of pure MoS_2, NC: Cu, and NC: O due to electronic transitions. In this methodology, the excited states are delineated as unoccupied Kohn−Sham states. The electric field of the photon instigates the transitions between the occupied and unoccupied states. The collective

https://doi.org/10.1021/acsomega.3c05213
ACS Omega 2023, 8, 37353−37368

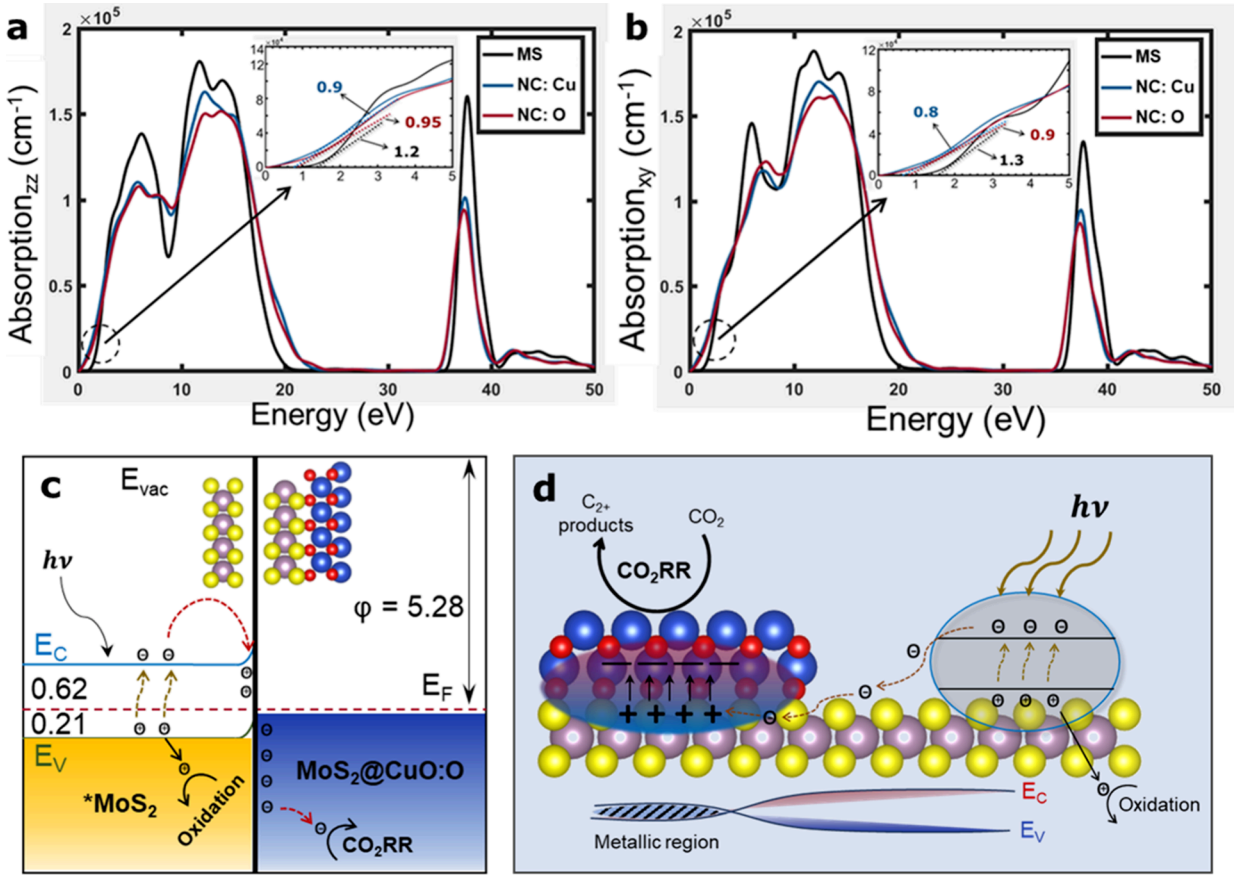

Figure 9. Optical absorption for MoS_2 (MS) slab, NC: Cu, and NC: O structures for light irradiation along (a) lateral (along the z axis) and (b) transverse (along the symmetric x, y axis) directions and photoenhanced electrocatalytic CO_2RR mechanism for both (c) lateral and (d) transverse cases.

excitations are known as plasmons. On the other hand, single particle excitations are considered independent transitions. The spectra that ensue from these excitations can be regarded as a joint DOS between the valence and conduction bands with appropriate matrix element weights.

A fraction of the total incident energy is lost as the wave passes through the material. This lost fraction is identified as the absorption coefficient, and it can be defined in terms of complex dielectric constants at a given frequency as $\varepsilon(\omega) = \varepsilon_r(\omega) + i\varepsilon_i(\omega)$, where $\varepsilon_r(\omega)$ and $\varepsilon_i(\omega)$ are the real and imaginary parts, respectively, and the absorption coefficient can be written as eq 12:

$$I(\omega) = \sqrt{2}\,\omega[\sqrt{\varepsilon_r(\omega)^2 + \varepsilon_i(\omega)^2} + \varepsilon_r(\omega)]^{1/2} \quad (12)$$

The absorption coefficient with positive magnitude can be achieved only when $\varepsilon_i(\omega) > 0$. $\varepsilon_i(\omega)$ can be represented as a full many-electron wave function as eq 13:[52]

$$\varepsilon_i(\hbar\omega) = \frac{2\pi e^2}{\Omega\varepsilon_0}\sum_{k,\nu,c} |\langle\psi_k^c|ur|\psi_k^\upsilon\rangle|^2\delta(E_k^c - E_k^\upsilon - E) \quad (13)$$

Here, Ω, ω, c, ν, and u are the total unit cell volume, frequency of incident photon, conduction bands (CBs), valence bands (VBs), and vectors defining incident electric field polarization, respectively. For materials that lack complete cubic symmetry, their optical characteristics will exhibit a certain degree of anisotropy. This feature can be incorporated into computations by considering the polarization of the electromagnetic field. As previously stated, the polarization orientation of the electric field is defined by the unit vector u.

From the analysis presented in Figure 9a, it is evident that the absorption coefficient exhibits a decrease for the entire range of photon energy when subjected to light irradiation along the z axis. Furthermore, a red shift toward lower energy is observed for both heterostructures as compared to the pristine MoS_2 slab model. This red shift will result in increased absorption of low energy photons in comparison to that of the MoS_2 surface slab. The optical band gaps (Figure 9a inset) are around 1.2 0.9 and 0.95 eV for MoS_2, NC: Cu, and NC: O. For irradiation along the transverse direction (Figure 9b), a similar behavior can be observed with optical band gaps (Figure 9b inset) of around 1.3 0.8, and 0.9 eV for MoS_2, NC: Cu, and NC: O, respectively.

The motion of the photogenerated electrons will vary depending on the direction. For the lateral direction (Figure 9c), the movement will occur between modified bulk *MoS_2 and the active NC: O heterostructure. Upon absorbing a photon, *MoS_2 generates electron−hole pairs. Most of the electrons instead of recombining with holes are transported to the active layer because of the intrinsic electric field. This electric field is induced because the work function of NC: O is slightly lower than *MoS_2. As a result, after coming into contact, the free electrons will transfer from *MoS_2 to NC: O until the Fermi levels are aligned and an equilibrium has been established. The induced electric field will propel the electrons from *MoS_2 to NC: O, and as a result, a positively charged

https://doi.org/10.1021/acsomega.3c05213
ACS Omega 2023, 8, 37353−37368

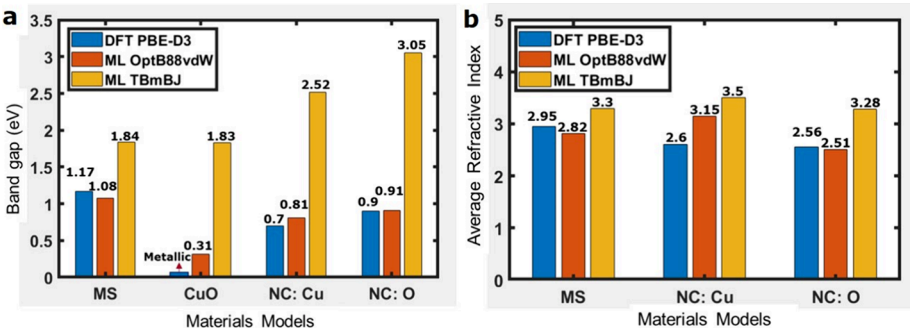

Figure 10. Comparison of (a) band gap and (b) average refractive index (averaged along the *x*, *y*, and *z* directions) calculated with the DFT method and JARVIS-ML for MoS_2, CuO, NC: Cu, and NC: O structures.

region is created at the *MoS_2 side. The positive region attracts the photogenerated electrons, and they are transported to the NC: O side quite quickly as they face an energy drop of around 0.62 eV due to SBH between *MoS_2 and NC: O. These energetic electrons are further propelled to Cu active sites because of the intrinsic electric field between MoS_2 and CuO in the NC: O active layer and participates in the CO_2 reduction reaction to form C_{2+} products.

For the transport of photogenerated electrons in the transverse direction, the NC: O heterostructure faces decreased sheet resistance due to CuO induced metallicity and overall lower electrostatic potential (Figure S4), and the transported electrons are propelled into the active surface because of the intrinsic vertical electric field. The contact resistance between these two regions is very low, as the work function of NC: O is 5.28 eV, which is very similar to the conduction band energy relative to the vacuum level of the adjacent MoS_2 sheet. A similar kind of low sheet resistance was observed with two phases of MoS_2 (1T-2H) with a contact resistance of 200−300 Ω μm.[53] The varying conductivity also means that the band gap is reduced from the pristine MoS_2 band gap toward zero band gap, and as a result, the nanostructure can absorb a wider range of energetic photons (0−1.2 eV). This is obvious from Figure 9a (inset) as the absorption coefficient slowly increases from zero to a high value for both NC: Cu and NC: O. In contrast, for the unmodified MoS_2, there is a sharp transition around 1.2 eV. Thus, the previously presented absorption values for the NC: Cu and O nanostructures were averages, and this wide range of absorption coefficient along the sheet means that they can absorb more of the sun energy spectrum.

Comparison between DFT and ML Predictions. We performed inference from the JARVIS-ML model on our model systems and compared them to the DFT calculations (Figure 10). The band gap and average refractive index were the target properties. According to the calculations, the predictions of the band gap from the ML-OptB88vdW model were closest to our DFT calculated values across all of the model systems considered (Figure 10a). The model predicted the lowering of the band gap even for the most physically unique 2D-CuO-(001) slab where it shows metallicity according to our DFT calculation. As the model was trained on nonmetallic 2D materials, it fails to predict out of distribution zero band gap for the model slabs. The ML-TBmBJ model overestimates all band gap values. For predicting the average refractive index, a similar outcome can be observed where ML-OptB88vdW model predictions come closer to the DFT values. According to the DFT calculations, both NC: Cu and O models show a refractive index lower than MoS_2. The ML-OptB88vdW model correctly predicts this trend for NC: O; however, it fails to do so for NC: Cu, where it predicts a refractive index higher than MoS_2. The predictions are overestimated by the ML-TBmBJ model; however, the difference is not drastic compared to the band gap predictions. Taking into account that the JARVIS-DFT model was trained on nonmetallic 2D materials and vdW heterostructures, the predictions were quite robust as the heterostructures in question are both metallic and non-vdW.

DISCUSSION

In this study, we performed detailed first-principle calculations to understand the effect of non-vdW heterostructure formation between the {001}-faceted CuO monolayer with different terminations and {002}-faceted MoS_2 bilayer on its structural (both surface and interface), charge distribution, electronic, and optical properties and how these changes can be used in the context of optically enhanced electrocatalytic reduction of CO_2 to suitable C_{2+} products.

From the binding energy, it is evident that the heterostructure formed between CuO and MoS_2 is stable and that MoS_2 can be used as a stabilizing support material for the active CuO monolayers as they face instability due to agglomeration in a reducing environment.[13] Because of the lack of any dangling bonds in the electron-filled sulfur atoms in MoS_2, the long-term stability of S edge in water has been theoretically shown.[14] This combined strong binding energy and intrinsic stability of MoS_2 are capable of protecting the CuO monolayer from the reducing environment by only exposing the active surface. The incorporation of {001}-faceted CuO monolayer also weakens the MoS_2 layer-to-layer attraction, resulting in destacking that in turn increases the active surface area.

For the active layer NC: O, reduction reactions are occurring continuously and thus require continuous supply of electrons that can be met because of the abundance of electrons on the CuO layer as has been shown by the layer-wise Bader calculation. Another insight from this calculation was that the oxidation state of surface copper atoms was lower than that of the bulk region. This result is important because it has been experimentally shown that locally reduced Cu atoms (i.e., lower oxidation state) are active for hydrogenation of *CO intermediate along with dimerization and protonation, which is an important step toward CO_2 reduction to C_{2+} products. A higher oxidation state such as Cu^{2+} oxide forms a copper carbonate passive layer hindering charge transport.[54] Moreover, a higher oxidation state is more selective toward

https://doi.org/10.1021/acsomega.3c05213
ACS Omega 2023, 8, 37353−37368

methane (CH_4) formation as the binding of *CO intermediate is stronger, and thus, further hydrogenation is possible especially with a solid solution with other metal oxides such as CeO_2.[55] Additionally, from the theoretical study, it was found that subsurface oxygen as present in the NC: O system stabilizes the physisorption of CO_2 molecules onto the Cu surface, which is the first step of the CO_2RR.[56] Thus, it is clear that the NC: O model system presents a suitable surface chemistry for CO_2RR to form C_{2+} products such as ethylene, ethanol, etc., selectively. Moreover, the reduction of low oxidation state Cu to Cu^0 is much slower than reduction of Cu^{2+} to Cu^+,[57] and the MoS2 nanosheets keep the CuO nanosheets separated, thus preventing dendritic Cu formation. However, without an efficient supply of electrons to the reducing active sites on the surface, the effectiveness of the active layer will suffer, and this charge transfer characteristic is captured by the Tafel slope, which is an important experimental screening factor to identify good catalysts.

The logarithmic form of the Tafel equation (eq 14), which is in turn a simpler version of the Butler−Volmer equation, linearly relates between electrode current density (j) and overpotential (η) as follows:

$$\log j = \log j_o + \frac{\alpha z F}{2.303RT}\eta \tag{14}$$

where the inverse of the factor before η, i.e., $\frac{2.303RT}{\alpha zF}$, is the Tafel slope, and it is clear that the Tafel slope has an inverse relation to the charge transfer coefficient (α). Thus, to achieve a small Tafel slope, good charge transferability is required. One of the defining factors of this charge transferability is different contact resistances in a catalytic cell.

Direct contact between MoS_2 and metal suffers from partial Fermi level pinning due to the interface dipole modified wave function near the metal contact and the presence of gap states near the MoS_2 layer.[58] Although vdW 2D heterostructures are a common choice for catalytic applications[59] and they have some advantages, for example, the SBH for a vdW heterostructure MS-G has been calculated to be only 0.18 eV,[60] physisorption type interactions between them cause a large tunneling barrier due to vdW gap, resulting in a large interfacial resistance.

The NC: Cu heterostructure has a smaller (5.28 eV) work function compared to 2D CuO (001): Cu slab (8.35 eV). Moreover, because of the high conductivity of the nanostructures due to CuO induced metallicity, no Fermi-level pinning in the absence of gap states between the contact material and the conductive layer unlike direct MoS_2-metal (Au, Cu, etc.) contact, and SBH assisted (0.62 eV) electron hopping from modified bulk MoS_2(*MoS_2) to NC: O heterostructures in the active layer, the electron transport is much more efficient. Thus, this heterostructure model is a suitable candidate for the conductive layer, where electrons can be easily injected from the metal cathode through the conductive layers to the active layers, as shown in the schematic in Figure 8b. For the active layer, the main concern is the swift transport of the hot electron coming from the conductive layer to the surface Cu sites, where the CO_2RR mainly occurs. The NC: O shows low tunneling barrier resistance due to chemisorption (no vdW gap like MS-G and MS-Bi), and the interfacial electric dipole induced bias controlled one-way flow of electrons from MoS_2 to CuO. The electron hopping between conductive layer and active layer is also efficient compared to layer-to-layer electron hopping in pristine MoS_2 nanoflower. The latter shows a large van der Waals gap induced potential barrier of around 4.33, 4.54, and 5.68 eV (Figure 8) for bulk MoS_2 to surface MoS_2, bulk MoS_2 to surface NC: Cu, and bulk MoS_2 to surface NC: O, respectively. Because of NC: Cu showcasing greater binding energy than NC: O, there is a high probability that NC: Cu is the dominant species in normal solution-based synthesis (solvothermal, hydrothermal, etc.) methods. However, this limitation assumes that we have an equal portion of Cu and O terminated CuO nanosheets. Moreover, they have two exposed surface area, and we can preferentially synthesize nanosheets with Cu termination on both surfaces using proper control of the synthesis conditions and utilizing recent development in bottom-up electrochemical synthesis of atomically thin TMOs based non-vdW nanostructures.[61]

Although the NC: O system does not directly fulfill the required energy level positions for both half reactions of photocatalytic reduction of CO_2, the spatially separated photogenerated carriers due to the intrinsic dipole[62] allocate extra electrons for the electrocatalysis CO_2RR reactions. This kind of Schottky enhanced photocatalysis has been validated experimentally for the CoP/g-C_3N_4 heterostructure, which is a similar metallic-semiconductor system.[63] In this case, the photoluminescence lifetime decreased because of rapid electron injection from semiconducting g-C_3N_4 to metallic CoP. This suppressed carrier recombination in g-C_3N_4 significantly enhanced the photocatalytic H_2 evolution performance.

CONCLUSIONS

In conclusion, MoS_2 based monolayer or bilayers are suitable support materials for active CuO monolayer due to good binding characteristic and good stability of MoS_2 in reducing conditions. The NC: Cu based heterostructure shows promise as a conductive support material for the main active material due to high conductivity, low interfacial resistances between external metal contact and the heterostructure (no Fermi level pinning), intralayer MoS_2 and CuO (low tunneling resistance), and interlayer conductive and active layers (SBH assisted electron hopping). For the NC: O based active layer, the combined effect of an interfacial electric field, low interface resistance, and active surface Cu sites with a low oxidation state with subsurface O atoms makes it a promising choice for the CO_2RR reaction for selective C_{2+} production. The electrocatalysis performance of our model system can be further enhanced through Schottky enhanced photocatalysis due to the good separation of photogenerated carriers. Thus, this study proposes a promising and unique heterostructure catalyst model that can be used in electrocatalytic reduction of CO_2 for selective production of C_{2+} products with a possible photo enhancement method. As the study solely focused on how the electrons behave in a chemical environment formed by chemisorption of the metallic CuO monolayer onto MoS_2, future studies should focus on the thermodynamics of this system for CO_2RR, specially to understand how this heterostructure changes the active surface sites and reaction pathways for the CO_2 conversion compared to only 2D-CuO nanosheets.

ASSOCIATED CONTENT

Supporting Information

The Supporting Information is available free of charge at https://pubs.acs.org/doi/10.1021/acsomega.3c05213.

https://doi.org/10.1021/acsomega.3c05213
ACS Omega 2023, 8, 37353−37368

Supercell structures with lattice parameters for (a) bilayer 2H-MoS_2 and (b) CuO and lattice planes showing preferential surface plane(s) for (c) 2H-MoS_2 (002) and (d) CuO (001) with both Cu and O terminations (Figure S1); 3D ELF isosurfaces for (a) NC: Cu and (b) NC: O models before and after the contact (Figure S2); PDOSs showing the (a) surface oxygen contribution to the NC: Cu model system and contributions from interfacial atoms (Cu, S) and (O, S) for (b) NC: Cu and (c) NC: O models, respectively (Figure S3); electrostatic potential profile for MoS_2 slab, NC: Cu, and NC: O models along direction *a* or *b* (symmetric) (Figure S4); and energy level diagram with work functions before contact for (a) NC: Cu and (b) NC: O models (Figure S5) (PDF)

AUTHOR INFORMATION

Corresponding Author

Ahmed Sharif − *Department of Materials and Metallurgical Engineering, Bangladesh University of Engineering & Technology, Dhaka 1000, Bangladesh;* orcid.org/0000-0002-1592-018X; Email: asharif@mme.buet.ac.bd

Authors

Md Rajbanul Akhond − *Department of Materials and Metallurgical Engineering, Bangladesh University of Engineering & Technology, Dhaka 1000, Bangladesh*

Md Jahidul Islam − *Department of Materials and Metallurgical Engineering, Bangladesh University of Engineering & Technology, Dhaka 1000, Bangladesh*

Ahmad Irfan − *Department of Chemistry, College of Science, King Khalid University, Abha 61413, Saudi Arabia*

Complete contact information is available at: https://pubs.acs.org/10.1021/acsomega.3c05213

Author Contributions

Md Rajbanul Akhond: Conceptualization, Calculations, Formal analysis, Writing − original draft. Md Jahidul Islam: Calculations, Formal analysis. Ahmad Irfan: Formal analysis, Writing − review and editing. Ahmed Sharif: Resources allocation, Supervision, Writing − review and editing.

Notes

The authors declare no competing financial interest.

ACKNOWLEDGMENTS

The authors would like to thank the Bangladesh University of Engineering and Technology (BUET) for providing assistance with computational facilities. A. Irfan extends his appreciation to the Deanship of Scientific Research at King Khalid University for funding through the Large Groups Project under grant number (RGP2/267/44).

REFERENCES

(1) *Key World Energy Statistics 2020 − Analysis*. IEA. https://www.iea.org/reports/key-world-energy-statistics-2020 (accessed 2023−07−09).

(2) *World Energy Outlook 2019 − Analysis*. IEA. https://www.iea.org/reports/world-energy-outlook-2019 (accessed 2023−07−09).

(3) Ye, R.-P.; Ding, J.; Gong, W.; Argyle, M. D.; Zhong, Q.; Wang, Y.; Russell, C. K.; Xu, Z.; Russell, A. G.; Li, Q.; Fan, M.; Yao, Y.-G. CO_2 Hydrogenation to High-Value Products via Heterogeneous Catalysis. *Nat. Commun.* **2019**, *10* (1), 5698.

(4) Roy, S.; Cherevotan, A.; Peter, S. C. Thermochemical CO_2 Hydrogenation to Single Carbon Products: Scientific and Technological Challenges. *ACS Energy Lett.* **2018**, *3* (8), 1938−1966.

(5) Kattel, S.; Liu, P.; Chen, J. G. Tuning Selectivity of CO_2 Hydrogenation Reactions at the Metal/Oxide Interface. *J. Am. Chem. Soc.* **2017**, *139* (29), 9739−9754.

(6) Gao, D.; Arán-Ais, R. M.; Jeon, H. S.; Roldan Cuenya, B. Rational Catalyst and Electrolyte Design for CO_2 Electroreduction towards Multicarbon Products. *Nat. Catal.* **2019**, *2* (3), 198−210.

(7) Tomboc, G. M.; Choi, S.; Kwon, T.; Hwang, Y. J.; Lee, K. Potential Link between Cu Surface and Selective CO_2 Electroreduction: Perspective on Future Electrocatalyst Designs. *Adv. Mater.* **2020**, *32* (17), 1908398.

(8) Kuhl, K. P.; Cave, E. R.; Abram, D. N.; Jaramillo, T. F. New Insights into the Electrochemical Reduction of Carbon Dioxide on Metallic Copper Surfaces. *Energy Environ. Sci.* **2012**, *5* (5), 7050−7059.

(9) Gattinoni, C.; Michaelides, A. Atomistic Details of Oxide Surfaces and Surface Oxidation: The Example of Copper and Its Oxides. *Surf. Sci. Rep.* **2015**, *70* (3), 424−447.

(10) Mishra, A. K.; Roldan, A.; de Leeuw, N. H. CuO Surfaces and CO_2 Activation: A Dispersion-Corrected DFT+U Study. *J. Phys. Chem. C* **2016**, *120* (4), 2198−2214.

(11) Zhou, K.; Wang, R.; Xu, B.; Li, Y. Synthesis, Characterization and Catalytic Properties of CuO Nanocrystals with Various Shapes. *Nanotechnology* **2006**, *17* (15), 3939.

(12) Su, D.; Xie, X.; Dou, S.; Wang, G. CuO Single Crystal with Exposed {001} Facets - A Highly Efficient Material for Gas Sensing and Li-Ion Battery Applications. *Sci. Rep.* **2014**, *4* (1), 5753.

(13) Wang, X.; Klingan, K.; Klingenhof, M.; Möller, T.; Ferreira de Araújo, J.; Martens, I.; Bagger, A.; Jiang, S.; Rossmeisl, J.; Dau, H.; Strasser, P. Morphology and Mechanism of Highly Selective Cu(II) Oxide Nanosheet Catalysts for Carbon Dioxide Electroreduction. *Nat. Commun.* **2021**, *12* (1), 794.

(14) Abidi, N.; Bonduelle-Skrzypczak, A.; Steinmann, S. N. How Stable Are 2H-MoS_2 Edges under Hydrogen Evolution Reaction Conditions? *J. Phys. Chem. C* **2021**, *125* (31), 17058−17067.

(15) Asadi, M.; Kumar, B.; Behranginia, A.; Rosen, B. A.; Baskin, A.; Repnin, N.; Pisasale, D.; Phillips, P.; Zhu, W.; Haasch, R.; Klie, R. F.; Král, P.; Abiade, J.; Salehi-Khojin, A. Robust Carbon Dioxide Reduction on Molybdenum Disulphide Edges. *Nat. Commun.* **2014**, *5* (1), 4470.

(16) Awasthi, G. P.; Poudel, M. B.; Shin, M.; Sharma, K. P.; Kim, H. J.; Yu, C. Facile Synthesis of a Copper Oxide/Molybdenum Disulfide Heterostructure for Asymmetric Supercapacitors of High Specific Energy. *J. Energy Storage* **2021**, *42*, No. 103140.

(17) Li, H.; Yu, K.; Lei, X.; Guo, B.; Li, C.; Fu, H.; Zhu, Z. Synthesis of the MoS_2 @CuO Heterogeneous Structure with Improved Photocatalysis Performance and H 2 O Adsorption Analysis. *Dalton Trans.* **2015**, *44* (22), 10438−10447.

(18) Wang, Y.; Tang, X.; Liu, Z.; Liu, Z.; Yan, Y.; Yang, B.; Zhu, Z. Fabrication of a Z-Scheme MoS_2/CuO Heterojunction for Enhanced 2-Mercaptobenzothiazole Degradation Activity and Mechanism Insight. *New J. Chem.* **2020**, *44* (42), 18264−18273.

(19) Jiang, F.; Ding, B.; Liang, S.; Zhao, Y.; Cheng, Z.; Xing, B.; Ma, P.; Lin, J. Intelligent MoS_2−CuO Heterostructures with Multiplexed Imaging and Remarkably Enhanced Antitumor Efficacy via Synergetic Photothermal Therapy/ Chemodynamic Therapy/ Immunotherapy. *Biomaterials* **2021**, *268*, No. 120545.

(20) Arunbalaji, S.; Vasudevan, R.; Arivanandhan, M.; Alsalme, A.; Alghamdi, A.; Jayavel, R. CuO/MoS2 Nanocomposites for Rapid and High Sensitive Non-Enzymatic Glucose Sensors. *Ceram. Int.* **2020**, *46* (10), 16879−16885.

(21) Wang, J.; Gao, Y.; Kong, H.; Kim, J.; Choi, S.; Ciucci, F.; Hao, Y.; Yang, S.; Shao, Z.; Lim, J. Non-Precious-Metal Catalysts for Alkaline Water Electrolysis: Operando Characterizations, Theoretical Calculations, and Recent Advances. *Chem. Soc. Rev.* **2020**, *49* (24), 9154−9196.

(22) Zhou, Y.; Silva, J. L.; Woods, J. M.; Pondick, J. V.; Feng, Q.; Liang, Z.; Liu, W.; Lin, L.; Deng, B.; Brena, B.; Xia, F.; Peng, H.; Liu, Z.; Wang, H.; Araujo, C. M.; Cha, J. J. Revealing the Contribution of Individual Factors to Hydrogen Evolution Reaction Catalytic Activity. *Adv. Mater.* **2018**, *30* (18), 1706076.
(23) Choudhary, K.; Garrity, K. F.; Hartman, S. T.; Pilania, G.; Tavazza, F. Efficient Computational Design of Two-Dimensional van Der Waals Heterostructures: Band Alignment, Lattice Mismatch, and Machine Learning. *Phys. Rev. Mater.* **2023**, *7* (1), No. 014009.
(24) Soon, A.; Todorova, M.; Delley, B.; Stampfl, C. Erratum: Thermodynamic Stability and Structure of Copper Oxide Surfaces: A First-Principles Investigation [Phys. Rev. B 75, 125420 (2007)]. *Phys. Rev. B* **2007**, *76* (12), No. 129902.
(25) Sheng, B.; Liu, J.; Li, Z.; Wang, M.; Zhu, K.; Qiu, J.; Wang, J. Effects of Excess Sulfur Source on the Formation and Photocatalytic Properties of Flower-like MoS_2 Spheres by Hydrothermal Synthesis. *Mater. Lett.* **2015**, *144*, 153−156.
(26) Zur, A.; McGill, T. C. Lattice Match: An Application to Heteroepitaxy. *J. Appl. Phys.* **1984**, *55* (2), 378−386.
(27) Di Liberto, G.; Morales-García, Á.; Bromley, S. T. An Unconstrained Approach to Systematic Structural and Energetic Screening of Materials Interfaces. *Nat. Commun.* **2022**, *13* (1), 6236.
(28) Hafner, J.; Kresse, G. The Vienna AB-Initio Simulation Program VASP: An Efficient and Versatile Tool for Studying the Structural, Dynamic, and Electronic Properties of Materials. In *Properties of Complex Inorganic Solids*; Gonis, A., Meike, A., Turchi, P. E. A., Eds.; Springer US: Boston, MA, 1997; pp 69−82. DOI: 10.1007/978-1-4615-5943-6_10.
(29) Kresse, G.; Joubert, D. From Ultrasoft Pseudopotentials to the Projector Augmented-Wave Method. *Phys. Rev. B* **1999**, *59* (3), 1758−1775.
(30) Blöchl, P. E. Projector Augmented-Wave Method. *Phys. Rev. B* **1994**, *50* (24), 17953−17979.
(31) Kresse, G.; Furthmüller, J. Efficient Iterative Schemes for Ab Initio Total-Energy Calculations Using a Plane-Wave Basis Set. *Phys. Rev. B* **1996**, *54* (16), 11169−11186.
(32) Anisimov, V. I.; Zaanen, J.; Andersen, O. K. Band Theory and Mott Insulators: Hubbard U Instead of Stoner I. *Phys. Rev. B* **1991**, *44* (3), 943−954.
(33) Hsu, H.; Blaha, P.; Wentzcovitch, R. M.; Leighton, C. Cobalt Spin States and Hyperfine Interactions in LaCoO3 Investigated by LDA+U Calculations. *Phys. Rev. B* **2010**, *82*, No. 100406, DOI: 10.1103/PhysRevB.82.100406.
(34) Hsu, H.; Umemoto, K.; Cococcioni, M.; Wentzcovitch, R. First-Principles Study for Low-Spin $LaCoO_3$ with a Structurally Consistent Hubbard-U. *Phys. Rev. B* **2009**, *79* (12), No. 125124.
(35) Krukau, A. V.; Vydrov, O. A.; Izmaylov, A. F.; Scuseria, G. E. Influence of the Exchange Screening Parameter on the Performance of Screened Hybrid Functionals. *J. Chem. Phys.* **2006**, *125* (22), 224106.
(36) Aryasetiawan, F.; Gunnarsson, O. The GW Method. *Rep. Prog. Phys.* **1998**, *61* (3), 237.
(37) Perdew, J. P.; Burke, K.; Ernzerhof, M. Generalized Gradient Approximation Made Simple. *Phys. Rev. Lett.* **1996**, *77* (18), 3865−3868.
(38) Islam, M. R.; Saiduzzaman, M.; Nishat, S. S.; Kabir, A.; Farhad, S. F. U. Synthesis, Characterization and Visible Light-Responsive Photocatalysis Properties of Ce Doped CuO Nanoparticles: A Combined Experimental and DFT+U Study. *Colloids Surf., A* **2021**, *617*, No. 126386.
(39) Grimme, S. Density Functional Theory with London Dispersion Corrections. *WIREs Comput. Mol. Sci.* **2011**, *1* (2), 211−228.
(40) Xiao, J.; Long, M.; Li, X.; Zhang, Q.; Xu, H.; Chan, K. S. Effects of van Der Waals Interaction and Electric Field on the Electronic Structure of Bilayer MoS_2. *J. Phys.: Condens. Matter* **2014**, *26* (40), No. 405302.
(41) Splendiani, A.; Sun, L.; Zhang, Y.; Li, T.; Kim, J.; Chim, C.-Y.; Galli, G.; Wang, F. Emerging Photoluminescence in Monolayer MoS_2. *Nano Lett.* **2010**, *10* (4), 1271−1275.
(42) Bagchi, S.; Ke, C.; Chew, H. B. Oxidation Effect on the Shear Strength of Graphene on Aluminum and Titanium Surfaces. *Phys. Rev. B* **2018**, *98* (17), No. 174106.
(43) Mugheri, A. Q.; Otho, A. A.; Mugheri, A. A. Meritorious Spatially on Hierarchically Co_3O_4/MoS_2 Phase Nanocomposite Synergistically a High-Efficient Electrocatalyst for Hydrogen Evolution Reaction Performance: Recent Advances & Future Perspectives. *Int. J. Hydrogen Energy* **2021**, *46* (44), 22707−22718.
(44) Ji, R.; Zhang, M.; Ma, W.; Zhu, Z.; Ma, C.; Huo, P.; Yan, Y.; liu, Y.; Li, C. Heterojunction Photocatalyst Fabricated by Deposition Co_3O_4 Nanoparticles on MoS_2 Nanosheets with Enhancing Photocatalytic Performance and Mechanism Insight. *J. Taiwan Inst. Chem. Eng.* **2019**, *97*, 158−169.
(45) Henkelman, G.; Arnaldsson, A.; Jónsson, H. A Fast and Robust Algorithm for Bader Decomposition of Charge Density. *Comput. Mater. Sci.* **2006**, *36* (3), 354−360.
(46) Zhang, W. X.; Yin, Y.; He, C. Lowering the Schottky Barrier Height of G/WSSe van Der Waals Heterostructures by Changing the Interlayer Coupling and Applying External Biaxial Strain. *Phys. Chem. Chem. Phys.* **2020**, *22* (45), 26231−26240.
(47) Koumpouras, K.; Larsson, J. A. Distinguishing between Chemical Bonding and Physical Binding Using Electron Localization Function (ELF). *J. Phys.: Condens. Matter* **2020**, *32* (31), No. 315502.
(48) Kulichenko, M.; Boldyrev, A. I. σ-Aromaticity in the MoS2Monolayer. *J. Phys. Chem. C* **2020**, *124* (11), 6267−6273.
(49) Li, C.; Fan, B.; Li, W.; Wen, L.; Liu, Y.; Wang, T.; Sheng, K.; Yin, Y. Bandgap Engineering of Monolayer MoS2 under Strain: A DFT Study. *J. Korean Phys. Soc.* **2015**, *66* (11), 1789−1793.
(50) Soon, A.; Todorova, M.; Delley, B.; Stampfl, C. Thermodynamic Stability and Structure of Copper Oxide Surfaces: A First-Principles Investigation. *Phys. Rev. B* **2007**, *75* (12), No. 125420.
(51) Shen, P.-C.; Su, C.; Lin, Y.; Chou, A.-S.; Cheng, C.-C.; Park, J.-H.; Chiu, M.-H.; Lu, A.-Y.; Tang, H.-L.; Tavakoli, M. M.; Pitner, G.; Ji, X.; Cai, Z.; Mao, N.; Wang, J.; Tung, V.; Li, J.; Bokor, J.; Zettl, A.; Wu, C.-I.; Palacios, T.; Li, L.-J.; Kong, J. Ultralow Contact Resistance between Semimetal and Monolayer Semiconductors. *Nature* **2021**, *593* (7858), 211−217.
(52) Read, A. J.; Needs, R. J. Calculation of Optical Matrix Elements with Nonlocal Pseudopotentials. *Phys. Rev. B* **1991**, *44* (23), 13071−13073.
(53) Kappera, R.; Voiry, D.; Yalcin, S. E.; Branch, B.; Gupta, G.; Mohite, A. D.; Chhowalla, M. Phase-Engineered Low-Resistance Contacts for Ultrathin MoS_2 Transistors. *Nat. Mater.* **2014**, *13* (12), 1128−1134.
(54) Velasco-Vélez, J.-J.; Jones, T.; Gao, D.; Carbonio, E.; Arrigo, R.; Hsu, C.-J.; Huang, Y.-C.; Dong, C.-L.; Chen, J.-M.; Lee, J.-F.; Strasser, P.; Roldan Cuenya, B.; Schlögl, R.; Knop-Gericke, A.; Chuang, C.-H. The Role of the Copper Oxidation State in the Electrocatalytic Reduction of CO_2 into Valuable Hydrocarbons. *ACS Sustainable Chem. Eng.* **2019**, *7* (1), 1485−1492.
(55) Zhou, X.; Shan, J.; Chen, L.; Xia, B. Y.; Ling, T.; Duan, J.; Jiao, Y.; Zheng, Y.; Qiao, S.-Z. Stabilizing Cu_{2+} Ions by Solid Solutions to Promote CO_2 Electroreduction to Methane. *J. Am. Chem. Soc.* **2022**, *144* (5), 2079−2084.
(56) Favaro, M.; Xiao, H.; Cheng, T.; Goddard, W. A.; Yano, J.; Crumlin, E. J. Subsurface Oxide Plays a Critical Role in CO_2 Activation by Cu(111) Surfaces to Form Chemisorbed CO_2, the First Step in Reduction of CO_2. *Proc. Natl. Acad. Sci.* **2017**, *114* (26), 6706−6711.
(57) Fan, Q.; Zhang, M.; Jia, M.; Liu, S.; Qiu, J.; Sun, Z. Electrochemical CO_2 Reduction to C_{2+} Species: Heterogeneous Electrocatalysts, Reaction Pathways, and Optimization Strategies. *Mater. Today Energy* **2018**, *10*, 280−301.
(58) Gong, C.; Colombo, L.; Wallace, R. M.; Cho, K. The Unusual Mechanism of Partial Fermi Level Pinning at Metal−MoS_2 Interfaces. *Nano Lett.* **2014**, *14* (4), 1714−1720.
(59) Deng, D.; Novoselov, K. S.; Fu, Q.; Zheng, N.; Tian, Z.; Bao, X. Catalysis with Two-Dimensional Materials and Their Heterostructures. *Nat. Nanotechnol.* **2016**, *11* (3), 218−230.

https://doi.org/10.1021/acsomega.3c05213
ACS Omega 2023, 8, 37353−37368

(60) Hieu, N. N.; Phuc, H. V.; Ilyasov, V. V.; Chien, N. D.; Poklonski, N. A.; Van Hieu, N.; Nguyen, C. V. First-Principles Study of the Structural and Electronic Properties of Graphene/MoS_2 Interfaces. *J. Appl. Phys.* **2017**, *122* (10), 104301.
(61) Ji, D.; Lee, Y.; Nishina, Y.; Kamiya, K.; Daiyan, R.; Chu, D.; Wen, X.; Yoshimura, M.; Kumar, P.; Andreeva, D. V.; Novoselov, K. S.; Lee, G.-H.; Joshi, R.; Foller, T. Angstrom-Confined Electrochemical Synthesis of Sub-Unit-Cell Non-Van Der Waals 2D Metal Oxides. *Adv. Mater.* **2023**, 2301506.
(62) Liu, X.; Cheng, P.; Zhang, X.; Shen, T.; Liu, J.; Ren, J.-C.; Wang, H.; Li, S.; Liu, W. Enhanced Solar-to-Hydrogen Efficiency for Photocatalytic Water Splitting Based on a Polarized Heterostructure: The Role of Intrinsic Dipoles in Heterostructures. *J. Mater. Chem. A* **2021**, *9* (25), 14515−14523.
(63) Wang, X. j.; Tian, X.; Sun, Y. j.; Zhu, J. y.; Li, F. t.; Mu, H. y.; Zhao, J. Enhanced Schottky Effect of a 2D−2D CoP/g-C_3N_4 Interface for Boosting Photocatalytic H_2 Evolution. *Nanoscale* **2018**, *10* (26), 12315−12321.

https://doi.org/10.1021/acsomega.3c05213
ACS Omega 2023, 8, 37353−37368